Available online at www.sciencedirect.com
ScienceDirect
International Journal of Heat and Mass Transfer 50 (2007) 3278–3290
International Journal of HEAT and MASS TRANSFER
www.elsevier.com/locate/ijhmt

Modeling of thermo-physical processes in liquid ceramic precursor droplets injected into a plasma jet

Saptarshi Basu, Baki M. Cetegen *

Mechanical Engineering Department, University of Connecticut, Storrs, CT 06269-3139, United States

Received 14 August 2006; received in revised form 26 January 2007
Available online 30 March 2007

Abstract

Modeling of liquid ceramic precursor droplets axially injected into a plasma is presented. Droplets undergo heating and solvent vaporization leading to high solute concentration near droplet surface. At a critical solute super-saturation concentration, precipitation is postulated to occur forming a precipitate shell around liquid core. Internal pressurization and rupture of shell occur subsequently. Droplet size, shell porosity and thickness effects were studied. Timescales of internal pressurization and precipitate formation are of the order of microsecond and millisecond, respectively. Small droplets ($d \leqslant 5$ μm) tend to form thick shells and are less likely to undergo shell fracture compared to larger droplets.

Keywords: Droplet/plasma interaction; Solute precipitation; Droplet heating; Vaporization; Ceramic precursors

1. Introduction

Production of high value materials in the form of powders and thin coatings is a large multi billion dollars manufacturing enterprise. Specific functional materials have been synthesized by different processes including spray drying and pyrolysis [1] as well as combustion and plasma processing [2]. Among the different processing techniques, plasma and high velocity oxy-fuel (HVOF) techniques [2] have been successfully employed for generation of high-value protective coatings on hardware components such as thermal barrier coatings on gas turbine blades and corrosion and wear resistant coatings in other applications. In all these, a powder of the coating material is typically heated in a plasma or HVOF jet to deposit partially or fully molten particles onto a substrate forming a thin coating [2].

An alternate route to this process is the injection of a liquid spray composed of droplets containing the dissolved salts of the materials to be deposited [3–8]. In this case, droplets, injected into a high temperature plasma or HVOF environment, vaporize and concentrate the salt solutes followed by heterogeneous or homogeneous nucleation of solid intermediates, their chemical transformations and melting before deposition on a substrate surface. This in-situ processing of liquid containing droplets in a high temperature environment critically determines not only the chemical make-up of the generated coatings but also its microstructural characteristics depending on the physico-chemical processes that occur at the droplet scale. For example, depending on the heating rate of droplets and the nature of precipitation during heat-up and vaporization phases, different particle morphologies are obtained including solid particles, hollow shells, and fragmented shells as schematically shown in Fig. 1. When droplets are small and the solute diffusivity is high, increase of solute concentration occurs uniformly throughout the droplet leading to precipitation throughout and consequent formation of solid particles as shown as path (A) in Fig. 1. When rapid vaporization occurs on the droplet surface and the solute diffusivity is low such that a high solute concentration builds up around the droplet periphery, as shown in path B in Fig. 1, there could be different outcomes including fragmented shells (B-I) as a result of internal pressurization

* Corresponding author. Tel.: +1 860 486 2966; fax: +1 860 486 5088.
E-mail address: cetegen@engr.uconn.edu (B.M. Cetegen).

0017-9310/$ - see front matter © 2007 Elsevier Ltd. All rights reserved.
doi:10.1016/j.ijheatmasstransfer.2007.01.036

Nomenclature

B_M	spalding mass transfer number, $B_M = (\chi_{v,\infty} - \chi_{v,s})/(1 - \chi_{v,s})$
B_T	spalding heat transfer number, $B_T = C_{p,v}(T_\infty - T_s)/(h_{lv} - Q_L/\dot{m})$
C_D	drag coefficient
C_p	specific heat
D_{12}	mass diffusivity of the vapor phase into plasma
D_s	mass diffusivity of Zirconium acetate into water
h_{lv}	latent heat of vaporization for liquid
F	film thickness factor due to surface blowing, $F(B) = (1+B)^{0.7}\ln(1+B)/B$
k	thermal conductivity
Le	Lewis number, $Le = D/\alpha$
$\dot{m}$	mass flow rate at the droplet surface due to vaporization
Nu^*	Nusselt number corrected for surface blowing $Nu^*=2+(Nu_o-2)/F(B_T)$
Nu_0	Nusselt number for a non-vaporizing sphere
Pr	Prandtl number, $Pr = \nu/\alpha$
$\dot{Q}_L$	heat transfer rate into the droplet surface
r_s	instantaneous outer radius of the droplet
$\bar{r}_s$	non-dimensional radius of the droplet, $\bar{r}_s = r_s/r_0$
Re	Reynolds number based on droplet radius and relative velocity between the plasma and droplet
Sh^*	Sherwood number corrected for surface blowing $Sh^* = 2 + (Sh_0 - 2)/F(B_M)$
Sh_0	Sherwood number for a non-vaporizing sphere
t	time
T	temperature
$\overline{T}$	non-dimensional temperature, $\overline{T} = (T - T_0)/T_0$
U	axial velocity of the droplet
U_∞	axial plasma velocity
ε	porosity of the solid shell formed
T_s	solid phase temperature
T_l	liquid phase temperature
T_v	vapor phase temperature
r_l	radius of the liquid core
δ	thickness of the shell
V_{pore}	velocity of vapor venting through the pore
A_{pore}	total area of the pores
χ	mass fraction in the before precipitation regime
χ_s	mass fraction in the liquid core after precipitation regime
$\overline{\chi}$	non-dimensional mass fraction, $\overline{\chi} = (\chi - \chi_0)/\chi_0$
η	non-dimensional radial coordinate, $\eta = r/r_s$
ν	kinematic viscosity
ρ	density
τ	non-dimensional time, $\tau = \alpha_L t/r_0^2$
σ	yield stress
p_v	vapor pressure inside the solid shell
p_∞	pressure outside the droplet
D_p	diameter of the spheres forming the solid precipitate
R	universal gas constant
λ	mean free path
r_0	initial droplet radius

Subscripts

0	initial value
l	liquid phase
v	vapor phase
s	solid phase
∞	far field

for low vapor permeability through the formed shell, hollow spherical shells (B-II) for the case of high permeability through the shell, or rapid disintegration of the shell containing some of the liquid leading to secondary atomization (B-III) as a result of rapid internal pressurization and shell rupture. Another path is that of formation of a elastic shell that inflates due to internal liquid vaporization and eventual rupture and collapse of the deformed shell (Path C in Fig. 1). The particle morphology obtained from droplets is sensitive to the solute chemistry, diffusivity and solute solubility, droplet size as well as the thermal history of droplets. Typically, high heating rates and large droplets tend to form hollow particles while small droplets at low heating rates generate solid particles. Fig. 2 shows the schematic of the droplet morphology. The typical initial droplet surface heating rates in a DC arc plasma or an oxy-fuel flame can range from 10^5 to 10^7 K/s which are much higher than those studied in the spray pyrolysis literature [9,10] which are typically 10^2 to 10^3 K/s.

1.1. Review of previous studies

The spray pyrolysis literature contains both experimental and modeling studies that have explored conditions under which different types of particles are formed. Messing et al. [9] and Jain et al. [10] reviewed this subject presenting both experimental data and modeling results pointing to the different morphologies. Che et al. [11] carried out studies in which the particle structure was controlled by reactions within the droplets in spray pyrolysis. They achieved dense or hollow single crystal or layered particle structures by carefully controlling the reactions within droplets, sintering and phase transformations. Zhang et al. [12] studied experimentally the formation of zirconia from different zirconium salts and determined the conditions and the types of precursor solutions that yield solid particles. Nimmo et al. [13] studied generation of zirconia from zirconium nitrate sprayed with a diameter of less than 5-μm into a controlled heating furnace. They

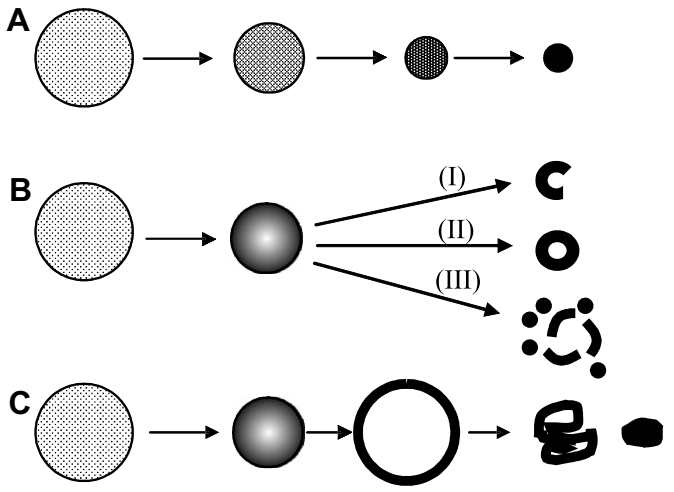

Fig. 1. Solute containing droplet vaporization and precipitation routes: (A) uniform concentration of solute and volume precipitation leading to solid particles; (B) super-saturation near the surface followed by (I) fragmented shell formation (low permeability through the shell, (II) unfragmented shell formation (high permeability), (III) impermeable shell formation, internal heating, pressurization and subsequent shell break-up and secondary atomization from the internal liquid; (C) elastic shell formation, inflation and deflation by solids consolidation.

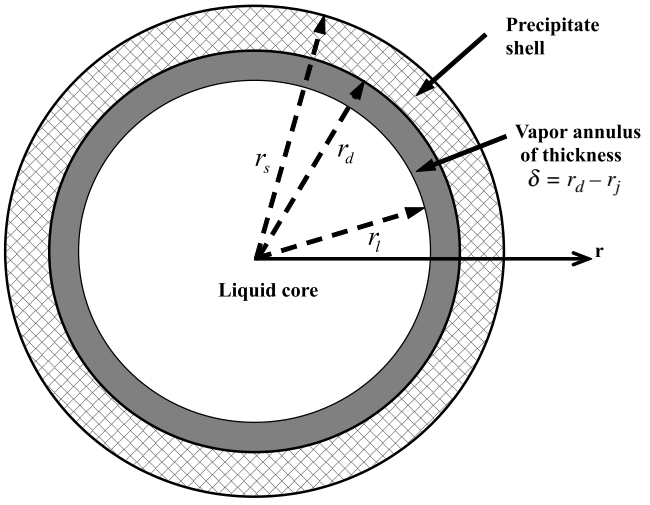

Fig. 2. Schematic of the droplet before and after precipitation.

were able to produce tetragonal phase ultrafine zirconia powers under certain operating conditions.

Linn and Gentry [14] performed an experimental study of single droplet precipitation of different aqueous solutions of calcium acetate, sodium acetate, sodium carbonate, ammonium chloride, lithium manganous nitrate and barium alumino silicate. They found that after a period of uniform shrinkage due to evaporation in a hot gas environment, crystallization, crust formation and fracture of the crust were observed. Ammonium chloride and lithium manganous nitrate showed bubbling and inflation of the precursor droplets after the initial shrinkage. While these studies illustrate the different nucleation, precipitate formation and in some cases inflation of droplets upon heating, these experiments are conducted at low heating rates where droplets are suspended in a relatively low gas temperature environment (with respect to flame or a plasma) and low velocities. Since the precipitation morphology is expected to be strongly dependent on the droplet heating rates, the actual processes taking place in a droplet can be altered significantly. Modeling of precipitation of solute salts in a liquid droplet has been primarily based on the homogeneous nucleation hypothesis [15]. It is assumed that onset of precipitation occurs when the solute concentration reaches a super-saturation level and engulfs all regions of the droplet that exceed the equilibrium saturation concentration. While fundamental studies of precipitation onset in solution droplets have been undertaken [16,17], these studies have revealed that the parameters affecting the precipitation onset are difficult to determine even for the simple single component solutions under well-controlled conditions. Models based on the minimization of the Gibbs energy have been considered to predict the onset of precipitation [16]. In practice, validity of homogeneous precipitation hypothesis is in question firstly due to the more likely possibility of the heterogeneous precipitation as a result of impurities and secondly because of the effects of very rapid heating of droplets.

Computational modeling of droplet vaporization, solute concentration and precipitation has been reported in the literature. Early studies by Fuchs [18] and Ranz and Marshall [19] included analytical studies of diffusion and evaporation in droplets. Due to the limitations of these studies such as constant droplet diameter during evaporation, more detailed solutions of droplet vaporization and the resulting solute concentration fields were obtained from numerical solutions [15]. Most of these studies only considered droplets vaporizing in a surrounding high temperature stagnant gas environment. Precipitation of the solute salts in these and other models is based upon attainment of a certain super-saturation concentration of the solute before the onset of precipitation followed by precipitation in all regions of the droplet that are above the equilibrium saturation concentration. This assumption of homogeneous precipitation has been used widely in modeling, yet its validity for different material systems and droplet heating conditions is uncertain.

Recently, Ozturk and Cetegen [20–22] published several articles on modeling of single droplet vaporization for droplets convecting in high temperature plasma or oxy-fuel combustion jets. In these models, a detailed numerical solution of temperature and concentration fields have been obtained and homogeneous precipitation hypothesis has been invoked to estimate precipitation zones in these droplets. Motivated by the large body of research in droplet combustion [23], these models accounted for the shear-induced internal flow recirculation within the droplet and its effects on precipitate morphology. These computations, carried out for aqueous solution of zirconium acetate, have revealed thin shell type morphologies for large droplets and solid particle morphologies for smaller than 5-μm droplets

under rapid plasma and flame heating conditions [21]. Qualitative evidence of these morphologies was found in single pass sample collection experiments performed in a flame environment [24].

Formation of a precipitate shell around a vaporizing droplet encapsulates that droplet which then undergoes further internal heating in the plasma or flame. Depending on the porosity and other physical characteristics (rigidity or ductility) of the formed precipitate shell, the internal heating and vaporization of the liquid within the shell could result in one of the scenarios identified in Fig. 1. In this article, we present a model that considers the thermo-physical processes occurring following the precipitate shell formation assuming the formed shell is rigid and can have different levels of porosity. In the following sections, we first briefly summarize the simplified liquid droplet model that was adopted from our earlier work. We then extend the model to formation of a vapor layer between the liquid core and the shell. We present results of the model computations for different initial droplet sizes injected axially into a DC-arc plasma jet. The paper is concluded by the key findings and possible particle morphologies that result from rapid heating processes in a plasma environment.

2. Model description

2.1. Vaporization and solute concentration leading to shell formation

This part of the model is the same as in Refs. [20–22] except that the internal recirculation within the droplet due to shear at the liquid–gas interface has been neglected. This simplification leads to spherically symmetric concentration and temperature distributions within the droplet and thus does not account for the fore-to-aft variations of these quantities within the droplets. The binary (solute + solvent) droplets are injected axially into a high temperature plasma jet where solvent portion of the droplet starts evaporating with simultaneous reduction in droplet size and increase in surface concentration of the solute. The considered droplets are composed of zirconium acetate (solute) dissolved in liquid water (solvent) with an initial zirconium acetate mass fraction of 0.2.

Droplet motion in the hot convective gas environment is governed by the droplet momentum equation given by [20–22],

$$\frac{\partial U}{\partial t} = \frac{3C_D}{8r_s}\frac{\rho_\infty}{\rho_L}|U_\infty - U|(U_\infty - U) \tag{1}$$

$$\frac{\partial V}{\partial t} = \frac{3C_D}{8r_s}\frac{\rho_\infty}{\rho_L}V^2, \tag{2}$$

where U, V are the droplet velocities in x and y directions, C_D is the drag coefficient due to the relative motion between the droplet and the surrounding hot gases with U_∞ being the free stream flow velocity, i.e., local plasma flow velocity. The change in the droplet radius is given by [20–22],

$$\frac{\partial r_s}{\partial t} = \frac{\dot{m}}{4\pi\rho_L r_s^2}, \tag{3}$$

where $\dot{m}$ is the mass rate of vaporization, ρ_L is the liquid density and r_s is the radius of the droplet. The drag coefficient, C_D, is modified for the surface blowing effects as [20–22],

$$C_D = \frac{24}{Re(1+B_M)}, \tag{4}$$

where $\mathrm{Re} = \frac{2\rho_\infty r_s \Delta V}{\bar{\mu}}$, with ΔV being the relative velocity between the droplet and the external flow. Continuum expressions for drag coefficient and Nusselt numbers were employed in this study since the calculated Knudsen numbers $Kn = \lambda/2r_0$ are below 10^{-2} even for the smallest droplets considered in this study.

Above set of equations require the mass vaporization rate, $\dot{m}$, which is obtained from the vapor and liquid phase analyses. The flow relaxation times for the liquid phase is typically much longer than the vapor phase, therefore, the vapor phase solution can be approximated as quasi-steady state. The mass vaporization rate can be calculated from heat and mass transfer rates at the droplet surface as [20–22],

$$\dot{m} = 2\pi\rho_g D_{12} r_s Sh^* \ln(1+B_M) \tag{5}$$

$$\dot{m} = 2\pi\frac{k_g}{c_{P,F}} r_s Nu^* \ln(1+B_T), \tag{6}$$

where D_{12} is the diffusivity of the vapor in the plasma gas while $C_{P,F}$ is the average heat capacity of the vapor near the surface of the droplet. B_M and B_T are Spalding's mass and heat transfer numbers as defined in the nomenclature. In Eqs. (5) and (6), Nusselt number, Nu^* and Sherwood number, Sh^* are based on the non-vaporizing sphere, modified for the vaporization effects because of the varying film thickness around the droplet. The mass vaporization rate $\dot{m}$ cannot be calculated explicitly since the Spalding heat and mass transfer numbers, B_T and B_M, include droplet surface temperature and vapor mass fraction that are determined as a part of the coupled liquid phase solution. These equations are supplemented with the Clausius–Clapeyron equation and Raoult's law to determine the mass vaporization rate, surface temperature and surface vapor concentration. The surface temperature and mass vaporization rate are then used as boundary conditions in the solution of the conservation of energy and species equations in the liquid phase. For small droplets less than 100-μm, surface tension forces maintain the droplets in spherical shape justifying the assumption of spherical symmetry. Under these assumptions, the conservation of solute mass and energy equations can be written in simplified form as [20–22],

$$Le_L \bar{r}_s^2 \frac{\partial \overline{\chi}}{\partial \tau} - 0.5 Le_L \frac{dr_s}{dt}\eta\frac{\partial \overline{\chi}}{\partial \eta} = \frac{1}{\eta^2}\frac{\partial}{\partial \eta}\left(\eta^2\frac{\partial \overline{\chi}}{\partial \eta}\right) \tag{7}$$

$$\bar{r}_s^2 \frac{\partial \overline{T}}{\partial \tau} - 0.5\frac{dr_s}{dt}\eta\frac{\partial \overline{T}}{\partial \eta} = \frac{1}{\eta^2}\frac{\partial}{\partial \eta}\left(\eta^2\frac{\partial \overline{T}}{\partial \eta}\right), \tag{8}$$

where following dimensionless quantities are employed: $\bar{r}_s = r_s/r_0$, $\tau = \alpha_L t/r_0^2$, $\eta = r/r_s$, $\overline{\chi} = (\chi - \chi_0)/\chi_0$ and $\overline{T} = (T - T_0)/T_0$, with r_0 is the initial radius, α_L is the liquid thermal diffusivity, t is time, r_s is the droplet surface radius, T is temperature with T_0 being the initial value and correspondingly χ being the solute mass fraction with χ_0 being its initial value. Le_L is the liquid phase Lewis number. The initial and boundary conditions within the droplet can be written as,

$$\left\{\frac{\overline{\chi}}{\overline{T}}\right\}(\tau = 0) = 0 \quad \text{and} \quad \frac{\partial}{\partial\eta}\left\{\frac{\overline{\chi}}{\overline{T}}\right\}\Big|_{\eta=0} = 0 \quad \text{and}$$

$$\frac{\partial}{\partial\eta}\left\{\frac{\overline{\chi}}{\overline{T}}\right\}\Big|_{\eta=1} = \begin{cases} \frac{\dot{m}}{2\pi r_s \rho_L D_s \chi_{z,0}} \\ \frac{\dot{Q}_L}{2\pi r_s k_L T_0}, \end{cases} \tag{9}$$

where $\dot{Q}_L$ is the heat flux to the droplet, k_L is the liquid conductivity, ρ_L is liquid density, D_s is the mass diffusivity of solute in solvent.The Nusselt and Sherwood numbers are defined as follows [20–22] for a non-vaporizing sphere

$$\begin{aligned} Nu_0 &= 1 + (1 + Re \cdot Pr)^{1/3} f \\ Sh_0 &= 1 + (1 + Re \cdot Pr)^{1/3} f \end{aligned} \tag{10}$$

where $Pr = \frac{\overline{\mu}}{\overline{C}_p \overline{k}}$; $Sc = \frac{\overline{\mu}}{\overline{\rho} D_{12}}$. The averaged property values are evaluated at $T_{surface} + \frac{1}{3}[T_\infty - T_{surface}]$.

The factor f in Eq. (10) is taken as $f = 1$ for $Re \leqslant 1$ and $f = Re^{0.077}$ for $Re > 1$. The Nusselt and Sherwood numbers are modified for surface blowing as,

$$\begin{aligned} Nu^* &= 2 + (Nu_0 - 2)/F_M \\ Sh^* &= 2 + (Sh_0 - 2)/F_T \end{aligned} \tag{11}$$

where $F_i = (1 + B_i)^{0.7} \frac{\ln(1+B_i)}{B_i}$. For each time step, B_M and B_T are found iteratively such that the vaporization rate, $\dot{m}$ from Eq. (5) and (6) are same. The heat flux at the droplet surface is given by

$$\dot{Q}_L = \dot{m}\left[\overline{C}_{p,vapor}\frac{(T_\infty - T_{surface})}{B_T} - h_{lv}\right], \tag{12}$$

where h_{lv} is the latent heat of vaporization. Once the solute concentration distribution is determined from the above analysis, onset of precipitation and its extent is based on the homogeneous precipitation hypothesis [15]. It is assumed that precipitation of the ceramic precursor (zirconium acetate salt) occurs once the droplet surface concentration reaches a critical super-saturation value. Once this occurs, all regions of droplet with solute concentrations greater than its equilibrium saturation value precipitate. While this precipitation mechanism is quite simplistic, it has been employed extensively in the spray pyrolysis literature for the lack of a better more detailed model. In the following, thermal models for subsequent processes are described.

2.2. Internal vaporization and pressurization

The model detailed above describes the physical processes until the onset of precipitation and formation of a precipitate shell. Subsequent to shell formation, further heating of the particle containing a liquid core is modeled as follows. The particle motion through the hot plasma is still governed by Eqs. (1) and (2) except that the particle size is now fixed to the outer diameter of the precipitate shell. The Nusselt number for the particle is obtained from Eq. (10) for the impervious shell and Eqs. (10) and (11) for the porous shell with vapor blowing through its surface. Heat flux into the particle is evaluated from,

$$\dot{Q}_L = 2\pi r_s(1 - \varepsilon) Nu^* \bar{k}(T_\infty - T_{surface}), \tag{13}$$

where ε is the shell porosity ($0 \leqslant \varepsilon < 1$). The model of the interior of the particle is divided into three zones: solid shell, liquid core and vapor annulus as schematically shown in Fig. 2.

2.3. Thermal model for the shell

The energy equation for the shell is written as,

$$\frac{\partial T_s}{\partial t} = \frac{\alpha_s}{r^2}\frac{\partial}{\partial r}\left[r^2\frac{\partial T_s}{\partial r}\right] \tag{14}$$

Boundary conditions are:

$$\begin{aligned} \text{At} \quad r = r_s, \quad & -4\pi r_s^2 k_{solid}(1 - \varepsilon)\frac{\partial T_s}{\partial r} \\ & = \dot{Q}_L - \rho_v \overline{C}_{p,v} T_{surface} A_{pore} V_{pore}, \end{aligned} \tag{15}$$

where $\rho_v \overline{C}_{p,v} T_{surface} A_{pore} V_{pore}$ designates the enthalpy carried away by the gas venting through the pores. A_{pore} is the area of the pores and V_{pore} is the velocity of the gas through the pores. For an impervious shell, this term is zero.

At $r = r_s - \delta$ (solid–vapor interface)

$$4\pi r^2 k_{solid}\frac{\partial T_s}{\partial r} = 4\pi r^2 k_{vapor}\frac{\partial T_v}{\partial r} \tag{16}$$

2.4. Thermal model for vapor annulus between shell and liquid core

Heat supplied to the particle from the plasma heats the solid shell and starts vaporizing the liquid within the shell and forms a vapor annulus between the shell and the liquid core. This vapor annulus grows with time while the liquid core size reduces towards the center. For the vapor annulus, assumed to be spherically concentric, energy equation is given by,

$$\frac{\partial T_v}{\partial t} = \frac{\alpha_v}{r^2}\frac{\partial}{\partial r}\left[r^2\frac{\partial T_v}{\partial r}\right] + \frac{r_d - r}{r_d - r_l}\frac{dr_l}{dt}\frac{\partial T_v}{\partial r}, \tag{17}$$

where r_d is the outer radius of the vapor layer while r_l is the radius of the liquid core. $\frac{dr_l}{dt}$ denotes the rate of decrease of the liquid core radius due to the vaporization process. Boundary conditions are:

$$\text{At} \quad r = r_s - \delta = r_d, \quad 4\pi r^2 k_{solid} \frac{\partial T_s}{\partial r} = 4\pi r^2 k_{vapor} \frac{\partial T_v}{\partial r} \tag{18}$$

$$\text{At} \quad r = r_l, \quad -4\pi r^2 k_l \frac{\partial T_l}{\partial r} + 4\pi r^2 \rho_v h_{lv} \frac{dr_l}{dt} = -4\pi r^2 k_{vapor} \frac{\partial T_v}{\partial r} \tag{19}$$

2.5. Model for the liquid core

The liquid core slowly gets depleted with time as more and more vapor is formed. The energy equation for the liquid is given by,

$$\frac{\partial T_l}{\partial t} = \frac{\alpha_l}{r^2} \frac{\partial}{\partial r}\left[r^2 \frac{\partial T_l}{\partial r}\right] + \frac{r}{r_l} \frac{dr_l}{dt} \frac{\partial T_l}{\partial r} \tag{20}$$

Boundary condition at $r = r_l$ is given by Eq. (19) and symmetry condition $\frac{\partial T_l}{\partial r} = 0$ is employed in the droplet center. The liquid phase species equation is given by,

$$\frac{\partial \chi_s}{\partial t} = \frac{D_s}{r^2} \frac{\partial}{\partial r}\left[r^2 \frac{\partial \chi_s}{\partial r}\right] + \frac{r}{r_l} \frac{dr_l}{dt} \frac{\partial \chi_s}{\partial r}, \tag{21}$$

where D_s is the mass diffusivity of the solute in the solution and χ_s is the mass fraction of solute in the solution. Boundary conditions are:

$$\text{At} \quad r = r_l, \quad -D_s \frac{\partial \chi_s}{\partial r} + \chi_s \frac{dr_l}{dt} = 0 \tag{22}$$

$$\text{At} \quad r = 0, \ \text{from symmetry}, \frac{\partial \chi_s}{\partial r} = 0 \tag{23}$$

2.6. Internal pressurization due to vaporization within the shell

Depending on the type of shell formed, it may or may not have any venting effect through the pores in the shell. However, for the general case of a shell of porosity ε, one can write the following mass balance equation for the vapor.

$$\frac{dm_v}{dt} = -\frac{dm_l}{dt} - \frac{dm_{out}}{dt}, \tag{24}$$

where the m_v is the vapor mass within the shell, m_l is the remaining core liquid mass and the last term is the rate of vapor mass leaving the porous shell. Assuming ideal gas law for the vapor phase,

$$\frac{dm_v}{dt} = \frac{V_v}{RT_v} \frac{dp_v}{dt} + \frac{p_v}{RT_v} \frac{dV_v}{dt}, \tag{25}$$

where V_v is the vapor volume, T_v is the average temperature of the vapor phase and p_v is the vapor pressure. $\frac{dV_v}{dt}$ is the rate of change of volume of the vapor phase and can be written as $4\pi r_l^2 \left|\frac{dr_l}{dt}\right|$. Also,

$$\frac{dm_l}{dt} = 4\pi r_l^2 \rho_l \frac{dr_l}{dt} \tag{26}$$

and

$$\frac{dm_{out}}{dt} = \rho_v A_{pore} V_{pore} \tag{27}$$

Combining Eqs. (25)–(27) results in,

$$\frac{dp_v}{dt} = \frac{RT_v}{V_v}\left[4\pi r_l^2 \rho_v \left|\frac{dr_l}{dt}\right| - 4\pi r_l^2 \rho_l \frac{dr_l}{dt} - \rho_v A_{pore} V_{pore}\right] \tag{28}$$

This equation gives an expression for the internal pressure rise as a function of the vapor velocity escaping through the pores and the rate at which the liquid front is receding towards the droplet center.

2.7. Vapor convection through porous shell

Eqs. (15) and (28) contain the unknown vapor velocity through the porous shell. This velocity is estimated from the Carman–Kozeny [25] equation given by

$$V_{pore} = \frac{p_v - p_\infty}{\delta} \frac{\varepsilon^3 D_p^3}{180\mu_v (1-\varepsilon)^2}, \tag{29}$$

where δ is the thickness of the shell, D_p is the diameter of the particulates forming the shell. It should be emphasized that this equation is valid only for spherical particles. This shows that with pressure increase within the droplet, vapor velocity through the pores increases linearly with the pressure difference. Eq. (29) allows closure for Eqs. (24)–(28) for calculating T_l, T_v, T_s, p_v, χ_s.

2.8. Shell fracture criterion

Internal pressurization of the shell due to vaporization of the liquid within it can lead to shell rupture or inflation depending on the type of shell that forms during precipitation. This obviously depends on the solute and solvent characteristics and the thermo-physical conditions under which the precipitation occurs. Considering the case of a solid precipitate shell, the simplest shell fracture criterion is related to the yield stress of the shell material. In this approach, the fracture criterion becomes,

$$p_v = \frac{2\delta\sigma}{r_s}, \tag{30}$$

where σ represents the yield stress of the material of the shell. While, it is difficult to prescribe the yield stress of a precipitate shell which may depend on a multitude of parameters, some estimates based on published pure solute oxide (such as zirconium oxide) yield stresses are useful to study possible outcomes.

In the following section, we present the results obtained from the model computations and discuss these results in the context of solution precursor plasma process.

3. Results and discussion

Four different droplet diameter of 5, 10, 20 and 40-μm were injected into a plasma flow field axially at a velocity of 12 m/sec. The velocity and temperature field of the plasma obtained from the experimental data of Semenov and Cetegen [26] were used in the calculations. Fig. 3 shows

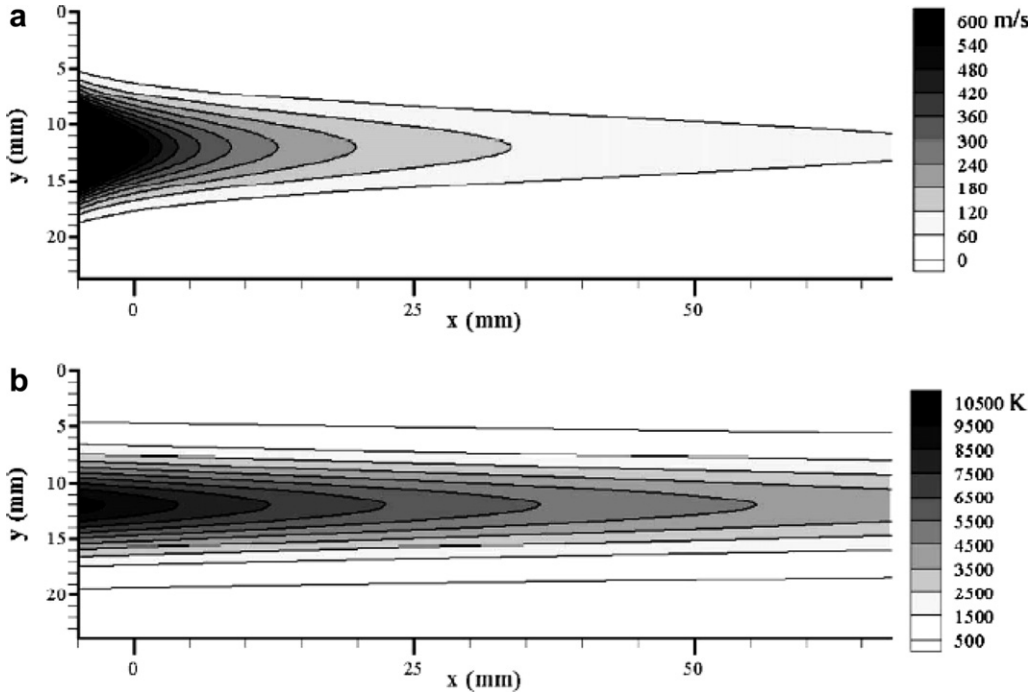

Fig. 3. Velocity field of the plasma in m/sec (a) and temperature field of the plasma in K (b).

the velocity and temperature distribution in a 38 kW DC arc plasma interpolated from the experimental data. At the exit of the plasma nozzle, velocity and temperature are in the range of 600 m/s and 10,000 K. Upon being injected axially into this plasma flow field, droplets follow straight line paths along the centerline of the plasma and undergo rapid heating and vaporization leading to decreasing droplet radius and increase in the surface concentration of the solute (zirconium acetate). Precipitation is triggered as soon as the surface mass fraction of the solute exceeds 0.95, which is taken as the critical supersaturation value for zirconium acetate. The precipitation is assumed to be instantaneous and all the parts of the droplet with mass fraction of solute greater than the saturation mass fraction (0.56) are assumed to precipitate forming a shell of varying thickness around the droplet with a liquid core.

Fig. 4 shows the radial distributions of temperature and mass fraction of solute within the droplet at the instant when precipitation is triggered for initial droplet diameters of 5, 10, 20 and 40-μm. In all cases, the temperature variation within the droplets is small as compared to the solute concentration variation as a consequence of the much larger thermal diffusivity compared to the solute mass diffusivity. As a result of more uniform increase in the solute concentration within the 5-μm droplet shown in Fig. 4a, a large region of the droplet is expected to precipitate as indicated by a 1.36-μm thick shell after droplet shrinkage of about 18% due to vaporization. The shell formation occurs after a residence time of 0.395 ms in the plasma. The shell region spans solute concentrations greater than $\chi_{Zr} \geqslant 0.56$.

For larger droplet sizes shown in Figs. 4b–d, the shell thickness can differ as a steeper solute concentration gradient develops in these larger droplets. For 10-μm initial size droplet as shown in Fig. 4b, 1.85-μm thick shell forms when the droplet radius reaches 4.2-μm at a residence time in the plasma of 1.18 ms. The maximum temperature at the droplet surface is 376.2 °C and is fractionally lower than that for the 5-μm droplet. For a 20-μm initial size droplet shown in Fig. 4c, mass fraction of the solute remains constant in the central part of the droplet to a radial distance of 7-μm. A precipitate shell of about 1-μm thickness forms when the droplet radius reaches 9.4-μm. The variation in temperature within the droplet is approximately 2 °C with the maximum temperature being about 6–7 °C lower than that for the 10-μm initial diameter droplet. The residence time of the 20-μm droplet in the plasma when the shell is formed is 1.66 ms. Fig. 4d shows the radial distribution of temperature and solute mass fraction for a 40-μm initial size droplet. The mass fraction of the solute remains constant at its initial value within a core of 15-μm radius. The formed shell is approximately 0.9-μm thick around the droplet of 18.8-μm radius at the instant of precipitation. The temperature variation within the droplet is about 2 °C with the maximum temperature being 7 °C lower than the 20-μm droplet. The residence time of the 40-μm droplet in the plasma until it forms the shell is 4.0 ms. It is clear from these results discussed above that smaller droplets form a precipitate shell faster than the larger droplets. The relative thickness of the shell when compared to the final radius of the droplet increases with decreasing initial droplet size. Droplet temperatures also reduce slightly with increasing droplet diameter.

The results predicted from the first part of the model provides the initial conditions for the second part of the model that involves heating of liquid precursor containing

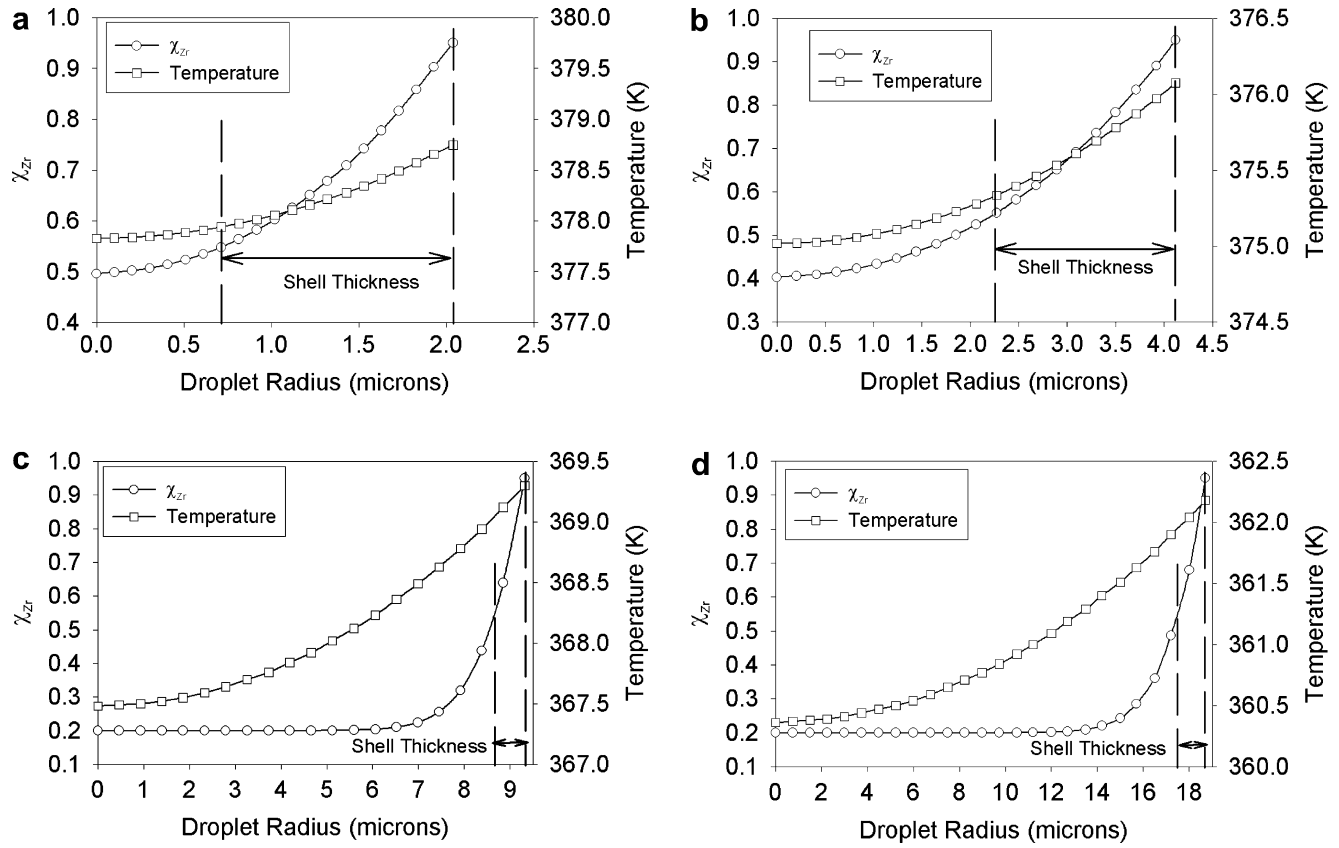

Fig. 4. Variation of mass fraction and temperature within 5-μm (a), 10-μm (b), 20-μm (c) and 40-μm (d) initial diameter droplets at onset of precipitation. The dotted lines signify the precipitated zone formed instantaneously.

shell. The shell thickness, droplet size, temperature and solute mass fraction are utilized for the next part of the model. Typically, the droplet temperatures and solute mass fractions are averaged and assumed constant throughout the liquid core for this part of the model. The plasma temperature and velocity fields are provided as inputs to the model as in the previous stage. No experimental data is available for the porosity of the precipitate shell formed around the liquid core in the plasma environment. Hence, a parametric study is performed for various levels of porosity to determine the effect of the porous shell structure on the build up of internal pressure and temperature within the particle.

Fig. 5a shows the internal pressure rise for a 10-μm initial diameter droplet for the impervious shell and for two levels of porosity. It is seen that the internal pressure rise is the fastest for the impervious shell since the impervious shell does not allow escape of any vapor from the particle. An initial rapid pressure rise occurs due to formation of the vapor layer between the liquid core and the shell. This is followed by continuous rise of pressure due to vaporization within the shell. For 20% porosity of the shell, the rate of pressure rise is reduced as compared to the impervious shell case due to venting of the formed vapor from the pores in the shell. For 40% shell porosity, the rate of pressure rise is much smaller after a relatively constant pressure period where rate of vapor generation and escape from the shell are equilibrated. In all cases, the internal pressure rise occurs over a period of microseconds as compared to the time scale of precipitate formation of milliseconds indicating a three orders of time separation between the two processes. Once the precipitate shell forms, the subsequent internal pressurization is almost instantaneous.

Fig. 5b shows the pressure rise behavior for 20-μm initial droplet diameter. As in the previous case, a rapid rise of pressure occurs initially followed by a more gradual increase depending on the porosity level. It is also observed that a pressure decay occurs in the early part of the process particularly for the porous shells. This is due to the fact that during the early stage the shell is not heated sufficiently enough to trigger a significant phase change in the liquid core leading to negligible pressure rise. However, as the liquid vaporization rate increases, the rate of vapor generation becomes greater than the counteracting venting effect through the pores. A glance at Eq. (28) confirms the fact that if the last term on the right hand side is larger than the combined sum of the first two terms which is the case during the early time period when $\frac{dr_l}{dt}$ is very low, then the pressure gradient may be negative. This is precisely what happens with increase in porosity as the term $\rho_v A_{pore} V$ increases with increase in A_{pore}, although this may not be physical.

Fig. 5c shows the pressure rise for a 40-μm initial diameter droplet. The trends are similar with the 20-μm droplet case except that the pressure rise occurs more slowly for the

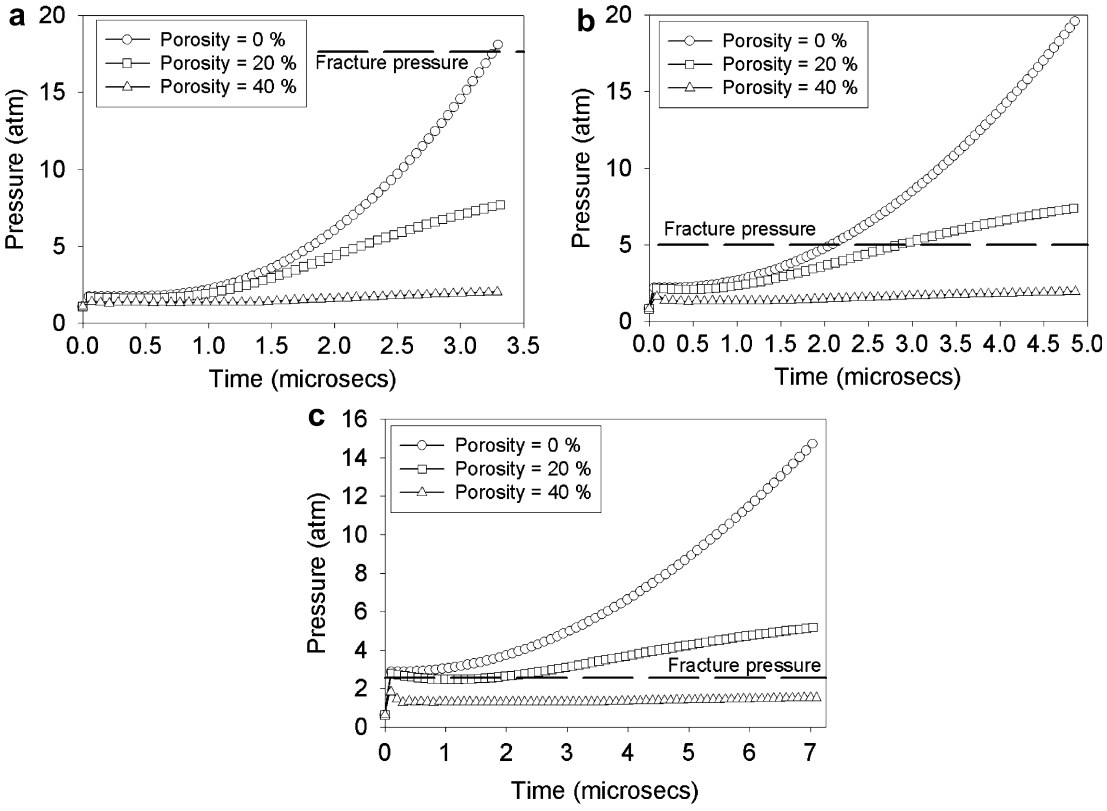

Fig. 5. Internal vapor pressure variation within the formed shell for 10-μm (a), 20-μm (b) and 40-μm (c) initial diameter droplets. Shell fracture pressures based on Eq. (30) are labeled for each size.

larger droplet. The main objective of calculating the internal pressure rise is to determine if and when the shell would fracture due to internal pressurization. While there is no quantitative data on the yield stress for the shell material, which may or may not be porous, an estimate of this can be based on the yield strength of amorphous zirconia shell material. Based on the values reported in the literature for the yield strength ($\sigma = 2$ Mpa), the internal pressure at which fracture is expected can be calculated from Eq. (30). These fracture pressure values are labeled in Fig. 5 and suggest that the fracture occurs at a higher internal pressure for the smallest droplet and decreases as the shell thickness relative to the droplet size decreases. For the 40-μm droplet based on the above yield strength and Eq. (30), an internal pressure of 2.5 atm is enough for shattering. However, we carried out the simulations up to a pressure rise of 15 atm as a very conservative estimate for fracture to occur. For 10-μm droplet the internal pressure rise needed for fracture is 18 atm while for the 20-μm droplets it is about 5 atm. Physically it is obvious that the porous shells will be weaker than the non-porous ones but due to the lack of experimental data, the same fracture criteria was used for all the cases irrespective of porosity. Although the "pre-precipitation" model gives us the shell thickness, it cannot predict the porosity of the shell formed. A special case of high fracture criteria of 40 atm was investigated for a 10-μm initial diameter non-porous droplet. The pressure rise was also computed for a 20% porous droplet of initial diameter 10-μm for a long duration.

Fig. 6a–c shows the temperature rise at three interface locations for nonporous shell as a function of time for different initial droplet sizes. It is seen that the surface temperature for each of the three droplet sizes increases almost linearly with time. This temperature rise is due to the fact that vaporization of the solvent from the droplet surface has ceased and all the heat transferred from the plasma is utilized for heating the outer shell. It is seen readily that the temperature at the droplet surface reaches the highest value of 440 °C for the 10-μm droplet while it is progressively lower for the larger size droplets. The temperature rises to only about 375 °C for the 40-μm droplet. The temperature at the vapor–solid interface shows almost linear temperature rise lagging behind the surface temperature after a short initial period of constant temperature. The maximum temperature rise is greatest for the 10-μm droplet and progressively diminishes for the larger sized droplets after the same time period. This is explained by the fact that as the smaller droplet precipitates quicker than the larger droplets, the temperatures of the plasma to which they are exposed after precipitation is much higher than the larger droplets which travel further downstream of the plasma jet where the temperature is lower thus leading to reduced heat transfer. The 40-μm droplet shows a much slower temperature increase that lags behind 10

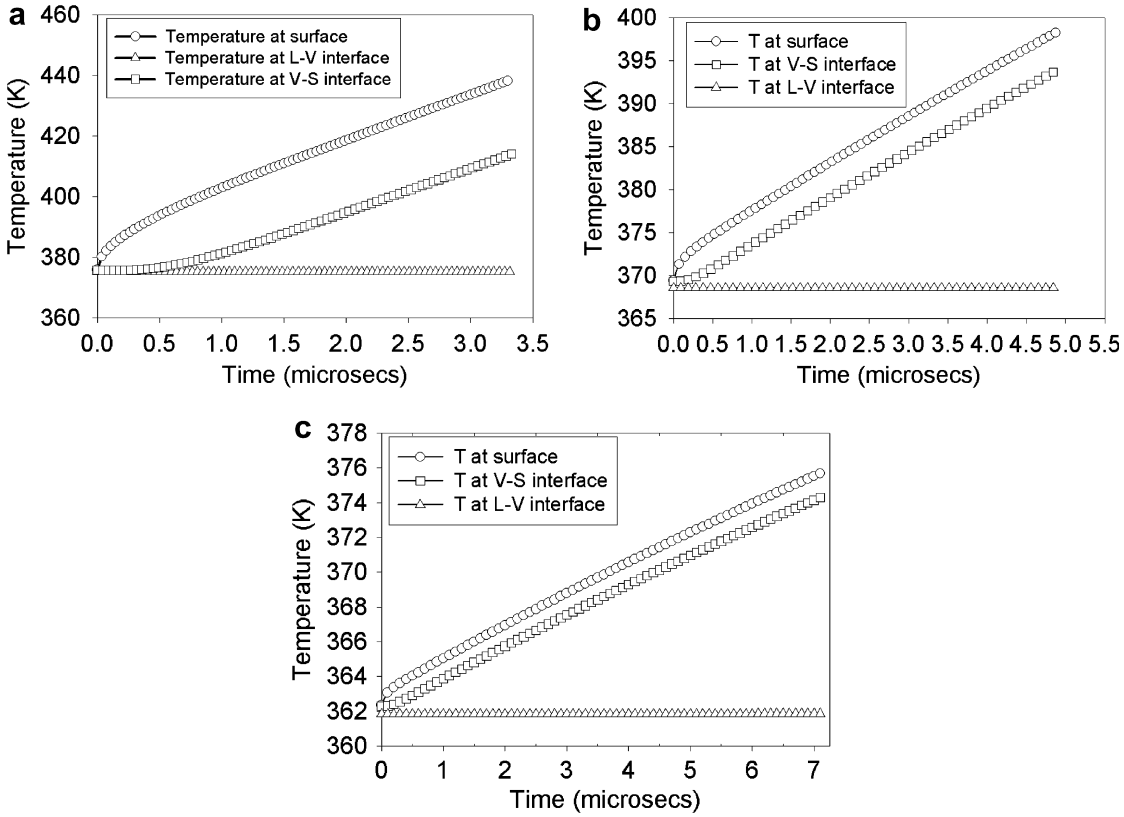

Fig. 6. Temperature variation at the shell surface, the vapor–solid interface and the liquid–vapor interface for 10-μm (a), 20-μm (b) and 40-μm (c) initial droplet diameters for non-porous shell.

and 20-μm droplets. The temperature at the liquid vapor interface shows very slight temperature increase for all the three droplet sizes as the majority of the heat is expended for phase change and only a small portion of the heat actually passes into the liquid core. This coupled with the high heat capacity of the liquid leads to an essentially constant temperature of the liquid interior.

Figs. 7a–c show the comparison of the temperature rise at the particle surface for varied levels of porosity for each of the three sizes. It is found that the effect of porosity and associated surface blowing of the vapor through the shell result in a decrease of shell surface temperature. This is due to two effects. First one is the surface blowing effect increasing the thickness of the thermal boundary layer and consequently reducing the heat transfer rate to the particle. This effect reduces the surface temperature of the droplet. Second effect is due to the heat carried out by the venting gas as this effect also reduces the heat transferred to the shell. For nonporous shell, both effects are absent. It is seen that the effect of porosity on surface temperature becomes more pronounced with the increasing droplet size. For a 10-μm droplet, the surface temperature rise is within 0.4 °C and it increases to maximum temperature deviations of about 1.5 and 2 °C for 20 and 40-μm droplets, respectively. It should also be noted that the 10-μm droplet is exposed to the hottest part of the plasma while the 20-μm and 40-μm droplets experience lower temperatures due to the greater time needed for precipitation.

Figs. 8a–c show the radial distributions of temperature and solute mass fraction for different levels of porosity. It is seen that the profiles for all levels of porosity for a 10-μm droplet shown in Fig. 8a, are indistinguishable. A significant temperature drop in the solid shell and a precipitous drop in the vapor film due to the low thermal conductivities are observed. However, in the small time scales of internal vaporization, the temperature of the liquid core rises by only 0.2 °C as is confirmed by the temporal variation of temperature near the vapor–liquid interface. Majority of the liquid core remains at the initial condition and is in a way shielded from the heat of the plasma by the solid shell and the vapor annulus. The mass concentration profiles show maximum rise at the liquid–vapor interface by about 0.010 from the base value of 0.45. Fig. 8b shows similar set of results for a 20-μm droplet. However, the temperatures in the solid shell decrease with increasing porosity but no significant difference is observed in the liquid and vapor phase temperature profiles. It is worth noting that a large temperature drop occurs in the shell, which is much thinner than the 10-μm case. The liquid core shows very small temperature increase while the vapor film shows a sharp temperature drop. Similar trends are found in Fig. 8c for a 40-μm droplet. The increase in mass concentration near the surface is about

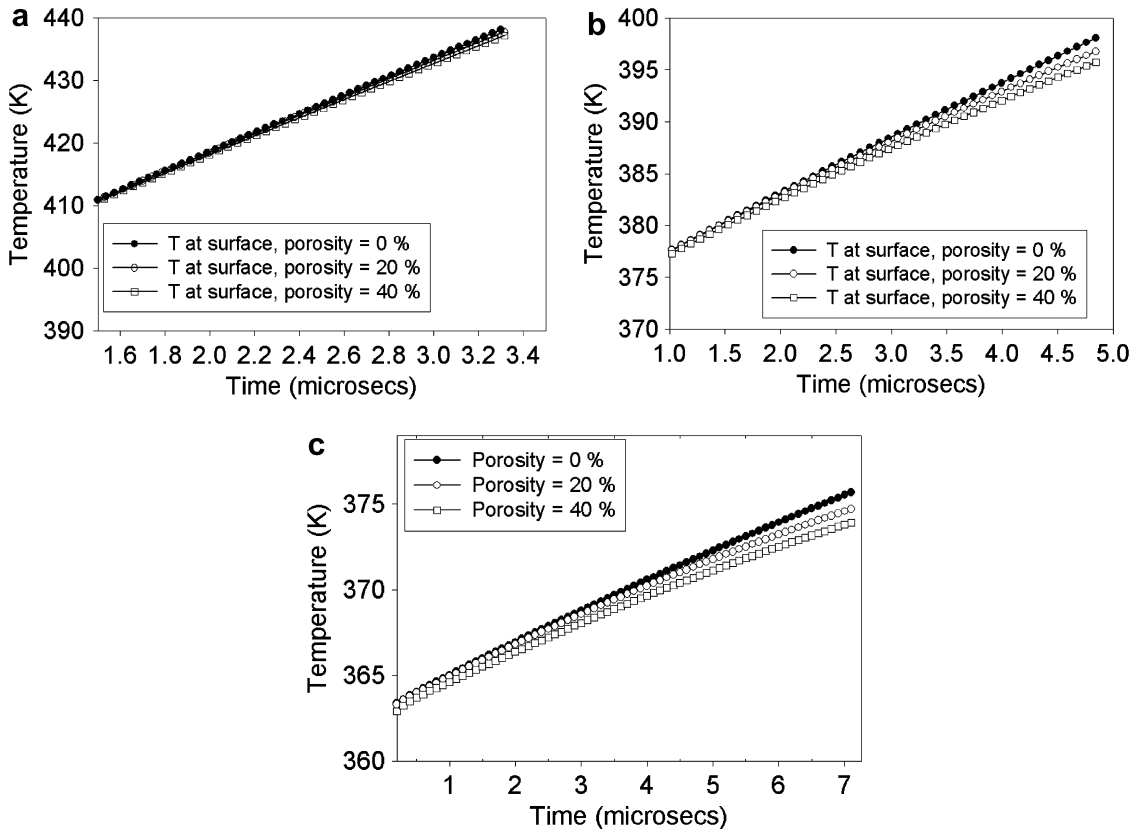

Fig. 7. Temperature variation with time at the shell surface for 10-μm (a), 20-μm (b) and 40-μm (c) initial droplet diameters for different levels of porosity.

0.02 for droplets of sizes 20 and 40-μm. No major differences in trends are found for different porosity levels except in the solid shell.

It is also of interest to determine the possibility of secondary precipitation, i.e. shell within a shell if the employed fracture criterion is different and the droplet can sustain high levels of internal pressure. 10-μm droplet with 0% and 20% porosity is chosen to study this effect. Fig. 9a shows that the internal pressure within a nonporous shell rises to 40 atm in about 4.4 microseconds. The internal pressure rises exponentially with increasing time. Fig. 9b shows the radial variation of the temperature and mass fraction profile within the shell at 4.4 microseconds. It is seen that the mass fraction at the liquid vapor interface has reached only 0.465 which is 0.015 above the initial value. The surface temperature rises to about 460 °C. Fig. 9c shows the pressure rise for a 20% porous shell exposed to the plasma for longer period of 12.5 microseconds as compared to the non-porous shell. The pressure rises to only about 18 atm with a diminishing rate after about 2 microseconds. The surface concentration of the solute rises to about 0.6 from the nominal value of 0.45 as shown in Fig. 9d suggesting that secondary precipitation inside the solid shell may occur at the liquid–vapor interface. The surface temperature rises to about 540 °C due to prolonged exposure to the plasma.

Once the internal pressure rises to a value at which the shell fracture is expected, the fate of the remaining liquid can only be speculated. While one can not describe the fragmentation of the liquid core quantitatively, a number of equal size droplets can be produced. Based on the conservation of the liquid volume at the time of shell rupture among these droplets, the new droplets would be of a diameter, $d_n = n^{-1/3} d_0$, where d_n is the diameter of the formed droplets and d_0 is the diameter of the liquid core. In the limiting case of the internal liquid dividing into a two droplets, each droplet diameter would be $0.79 d_0$, yielding the following droplet sizes. For 10-μm initial droplet diameter, divided droplets would be 3.2-μm diameter. Considering that the solute concentration is high in these liquid droplets, they will form solid spheres upon being further exposed to the plasma flow field. For 20-μm initial droplet diameter, each of the two formed droplets would be 12.8-μm in diameter. Given the low solute mass fraction in the parent droplet (see Fig. 4c), it is expected that the child droplets will undergo a secondary precipitation and shell formation. For the 40-μm initial droplet size, each child droplet would have a diameter of about 28-μm and they would also undergo secondary precipitation and shell formation. However, for these larger initial size droplets, if more than two droplets are formed during the shell rupture, the resulting smaller droplets may undergo volumetric precipitation and thus form solid particles. In experiments where plasma processed precursor was deposited on a substrate, it has been found that fractured hollow spherical shells and small spherical particles are omnipresent. These

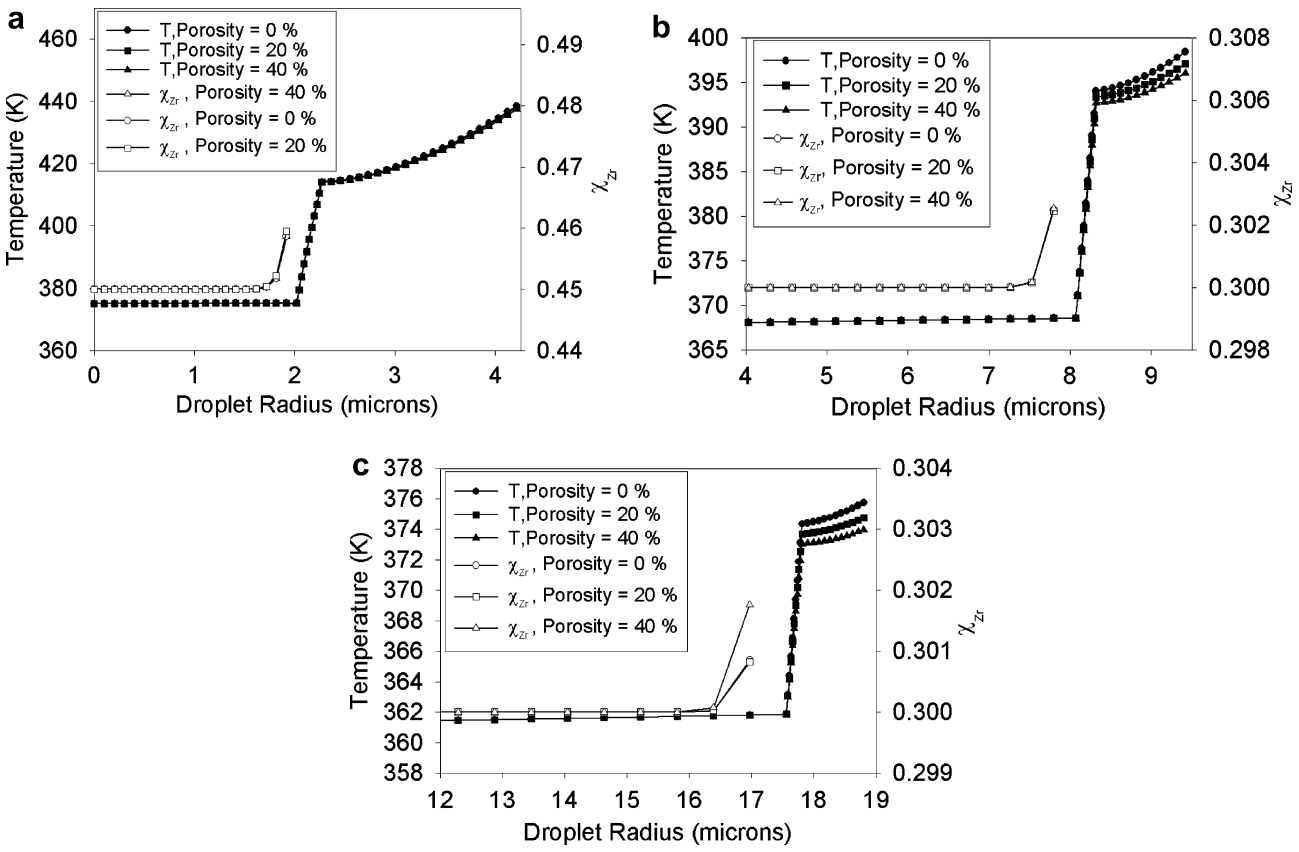

Fig. 8. Temperature and zirconia mass fraction variation along droplet radius for 10-μm (a), 20-μm (b) and 40-μm (c) initial droplet diameters for different levels of porosity.

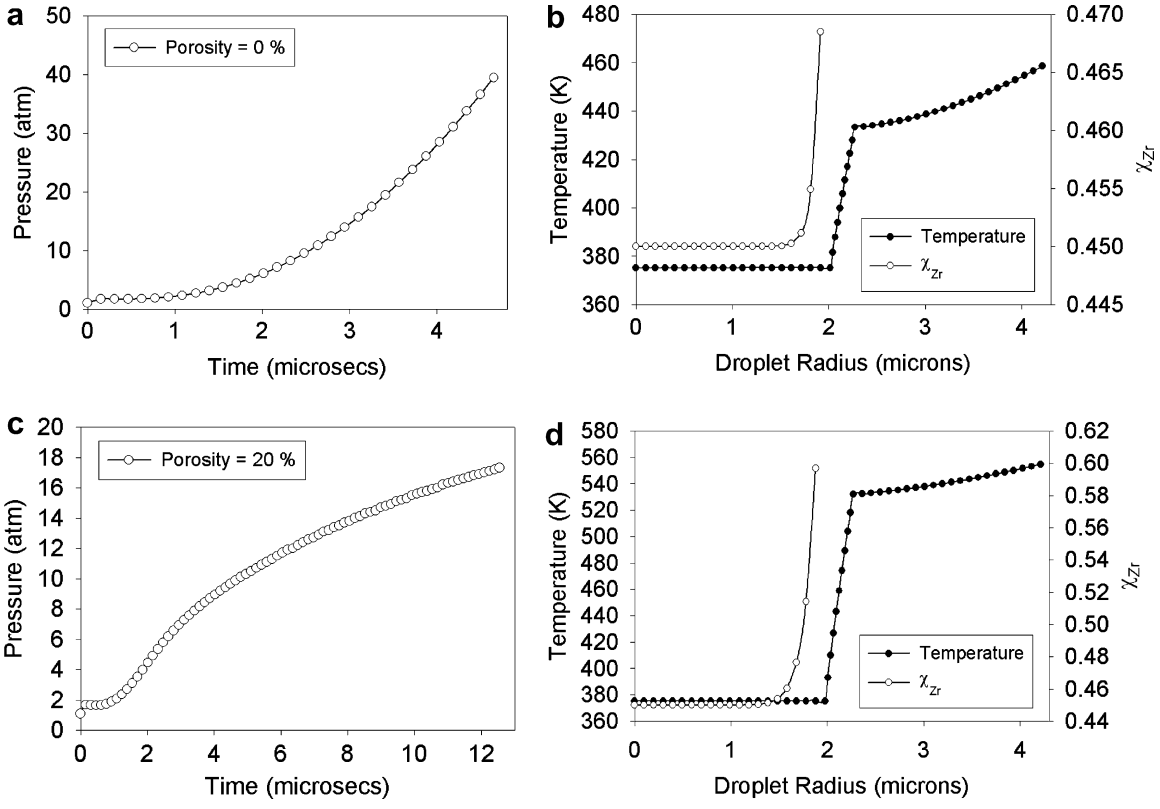

Fig. 9. Internal pressure rise (a) and temperature and zirconia mass fraction (b) for a 10-μm initial droplet diameter with a impervious shell for a fracture criteria of 40 atm; (c) and (d) are those for 10-μm initial droplet diameter with 20% porous shell.

observations provide a qualitative credibility of the model results discussed here.

4. Concluding remarks

A detailed model for liquid droplets injected axially into a thermal plasma jet has been presented in this article. The injected liquid ceramic precursor droplets first undergo vaporization and solute concentration within the vaporizing droplet leading to formation of a precipitate shell. Once formed, further heating of the droplet interior results in the formation of a vapor annulus and eventual rupture of the shell if it is sufficiently impervious to the vapor escape. Model results were obtained for different initial diameter precursor droplets composed of water and zirconium acetate. It is found that the smallest size droplets rapidly form a thick precipitate shell. Temperature distribution within droplets prior to precipitation is almost uniform while the solute mass fraction shows a significant variation near the droplet surface, particularly for the larger size droplets. In the post precipitation stage, the surface temperature of the smallest droplet rises more rapidly than the larger droplets and internal vapor pressure rises depending on the porosity of the formed precipitate shell. The droplet is assumed to fragment at a particular value of fracture strength based on the internal pressure rise and shell thickness. As expected, the highly porous shell vents the formed vapor and reduces the pressure rise significantly. Heating rate is not significantly affected due to porosity except in the solid shell. Upon fracture of the shell, it is expected that the internal liquid core is divided into a number of smaller droplets. Those originating from the smaller initial size droplets (10-μm and less) are predicted to form solid spheres as they would undergo volumetric precipitation after shell rupture. For larger size droplets such as 20 and 40-μm, secondary surface precipitation or volumetric precipitation may be expected depending on the number of droplets formed.

Acknowledgement

The research reported here was supported by the Office of Naval research, Grant No. N00014-02-1-0171 under the direction of Dr. Larry Kabacoff. We acknowledge the stimulating discussions with Prof. Eric Jordan (University of Connecticut) and Prof. Nitin Padture (Ohio State University) during the course of this research.

References

[1] K. Masters, Spray Drying handbook, forth ed., John Wiley & Sons, New York, 1985.
[2] L. Pawlowski, The Science and Engineering of Thermal Spray Coatings, John Wiley & Sons, Chihester, England, 1995.
[3] N.P. Padture, K.W. Schlichting, T. Bhatia, A. Ozturk, B.M. Cetegen, E.H. Jordan, M. Gell, Towards durable thermal barrier coatings with novel microstructures deposited by solution-precursor plasma spray, Acta Mater. 49 (2001) 2251–2257.
[4] E.H. Jordan, L. Xie, X. Ma, M. Gell, N.P. Padture, B.M. Cetegen, A. Ozturk, J. Roth, T.D. Xiao, P.E. Bryant, Superior thermal barrier coatings using solution precursor plasma spray, J. Therm. Spray Technol. 13 (1) (2004) 57–65.
[5] T. Bhatia, A. Ozturk, L. Xie, E. Jordan, B.M. Cetegen, M. Gell, X. Ma, N. Padture, Mechanisms of ceramic coating deposition in solution-precursor plasma spray, J. Mater. Res. 17 (9) (2002) 2363–2372.
[6] N. Padture, M. Gell, E.H. Jordan, Thermal barrier coatings for gas turbine engine applications, Science 296 (2002) 280–284.
[7] A. Ozturk, B.M. Cetegen, Experiments on ceramic formation from liquid precursor spray axially injected into an oxy-acetylene flame, Acta Mater. 53 (2005) 5203–5211.
[8] M. Gell, L. Xie, X. Ma, E.H. Jordan, N. Padture, Highly durable thermal barrier coatings made by the solution precursor plasma spray process, Surface Coat. Technol. 177-178 (2004) 97–102.
[9] G.L. Messing, S.C. Zhang, G.V. Jayanthi, Ceramic powder synthesis by spray pyrolysis, J. Am. Ceram. Soc. 76 (1993) 2707–2726.
[10] S. Jain, D.J. Skamser, T.T. Kodas, Morphology of single-component particles produced by spray pyrolysis, Aerosol Sci. Technol. 27 (1997) 575–590.
[11] S. Che, O. Sakurai, K. Shinozaki, N. Mizutani, Particle structure control through intraparticle reactions by spray pyrolysis, J. Aerosol Sci. 29 (3) (1998) 271–278.
[12] S.-C. Zhang, G.L. Messing, M. Borden, Synthesis of solid, spherical zirconia particles by spray pyrolysis, J. Am. Ceram. Soc. 73 (1) (1990) 61–67.
[13] W. Nimmo, D. Hind, H.J. Ali, E. Hampartsoumian, S.J. Milne, The production of ultrafine zirconium oxide powders by spray pyrolysis, J. Mater. Sci. 37 (2002) 3381–3387.
[14] J.-C. Lin, J.W. Gentry, Spray drying drop morphology: experimental study, Aerosol Sci. Technol. 37 (2003) 15–32.
[15] G.V. Jayanthi, S.C. Zhang, G.L. Messing, Modeling of solid particle formation during solution aerosol thermolysis, Aerosol Sci. Technol. 19 (1993) 478–490.
[16] M.D. Cohen, R.C. Flagan, J.H. Seinfeld, Studiues of concentrated electrolyte solutions using the electrodynamic balance: solution nucleation, J. Phys. Chem. 91 (1987) 4583–4590.
[17] K.H. Leong, Morphological control of particles generated from the evaporation of solution droplets: theoretical considerations, J. Aerosol Sci. 18 (5) (1987) 511–524.
[18] N.A. Fuchs, Evaporation and Droplet Growth in Gaseous Media, Pergamon Press, New York, 1959.
[19] W.E. Ranz, W.R. Marshall, Chem. Eng. Prog. 48 (1952) 173.
[20] A. Ozturk, B.M. Cetegen, Modeling of plasma assisted formation of ytrria stabilized zirconia from liquid precursors, Mat. Sci. Eng. A 384 (2004) 331–351.
[21] A. Ozturk, B.M. Cetegen, Modeling of axially and transversely injected precursor droplets into a plasma environment, Int. J. Heat Mass Trans. 48 (21–22) (2005) 4367–4383.
[22] A. Ozturk, B.M. Cetegen, Modeling of axial injection of ceramic precursor droplets into an oxy-acetylene flame environment, Mat. Sci. Eng. A 422 (1–2) (2006) 163–175.
[23] W.A. Sirignano, Fluid Dynamics and Transport of Droplets and Sprays, Cambridge University Press, 1999.
[24] A. Ozturk, B.M. Cetegen, Morphology of ceramic particulates formed in a premixed oxygen/acetylene flame from mono-size liquid precursor droplets, Acta Mater. 53 (2005) 2531–2544.
[25] J. Kozeny, Uber kapillare Leitung des Wassers im Boden, S. Ber.Weiner Akad, Abt. IIa 136 (1927) 271.
[26] S.Y. Semenov, B.M. Cetegen, Spectroscopic temperature measurements in DC-arc plasma jets utilized in thermal spray processing of materials, J. Therm. Spray Technol. 10 (2) (2001) 326–336.